npj | 2D materials and applications

www.nature.com/npj2dmaterials

ARTICLE OPEN

Check for updates

Abnormal thickness-dependent magneto-transport properties of vdW magnetic semiconductor $Cr_2Si_2Te_6$

Yun Li[1,2,3], Zheng Chen[3], Jie Wang[3,4], Teng Ii[3], Mingliang Tian[3,5], Julie Karel[1,2]✉ and Kiyonori Suzuki[2]✉

$Cr_2Si_2Te_6$ (CST) is a van der Waals (vdW) ferromagnetic semiconductor. The unique spin model and temperature-dependent magnetic ordering of CST provide opportunities for the next generation of two-dimensional (2D) spintronic devices. Here, abnormal magneto-transport properties are found in CST nanoflakes with variations in thickness. Interestingly, the thickness-dependent magnetoresistance (MR) effect exhibits a nonlinear change as a function of the magnetic field, temperature, and thickness. At a certain temperature below Curie temperature (T_c), a sign reversal of MR ratio from positive to negative can even be detected with thickness reduction. At the temperature range from T_c to 60 K, the Hall effect also presents a transformation from nonlinear behavior in thick layer CST to linear behavior in thin layer CST. These distinctive magneto-transport properties are attributed to the variation of spin correlation with thickness in CST nanoflakes. These findings probe the unique magneto-transport properties of CST and associate it with ferromagnetic correlation, which provides a basis for subsequent spintronics device design based on this material. This work also offers new insights into the relationship between sample thickness, transport properties, and spin correlation of other vdW ferromagnets. It lays a foundation for future vdW magnet-based device fabrication and possible spintronic applications.

npj 2D Materials and Applications (2023)7:39 ; https://doi.org/10.1038/s41699-023-00404-1

INTRODUCTION

The research on van der Waals (vdW) layered ferromagnets probes the physics of magnetic correlations and enables the development of nanoscale spintronic applications. Since the first demonstration of intrinsic 2D magnetism in atomically thin CrI_3[1] and $Cr_2Ge_2Te_6$[2] in 2017, the family of vdW ferromagnets has explosive growth and includes both ferromagnetic metals[3–5] and semiconductors[6,7]. The presence of uniaxial magneto-crystalline anisotropy in a spin-ordered state is the origin of intrinsic long-range magnetic ordering[2]. The weak interlayer interactions in the magnetic vdW crystal simplify the process of obtaining a few layers or monolayer nanoflakes by mechanical exfoliation[8]. 2D magnetic materials are mainly characterized by their significant thickness dependence[9–11]. Due to their larger specific surface area compared to conventional three-dimensional (3D) materials, 2D materials are more sensitive to external stimuli such as light and electricity[12–14]. The properties of these materials can be detected and regulated by a variety of optical, electrical and magnetic means for ultra-thin systems[15–17]. Numerous applications have emerged based on magneto-electric and magneto-optoelectronic properties[12,18–21]. By creating heterostructures using other stacked vdW materials[22,23], forming magnetic tunnel junctions[24–26] and novel functional devices have been achieved. For example, spin–orbit torques have been achieved in metal—$Cr_2Ge_2Te_6$ heterostructures resulting in field-assisted magnetization switching to the out-of-plane magnetization[27–30]. However, $Cr_2Si_2Te_6$ (CST) as a ferromagnetic semiconductor in the same material family of $Cr_2Ge_2Te_6$ has attracted less attention from researchers, due to its reduced stability in air[31], higher Curie temperature[32], and unexplored magnetic and transport properties. It has perpendicular magnetic anisotropy, temperature-dependent magnetic ordering, and a unique Ising spin model that is different to $Cr_2Ge_2Te_6$[33]. The controversial magneto-transport results in CST single crystals are still under debate, and there are no relevant reports based on the magneto-electric properties and spintronic applications of its nanoflakes[34,35].

CST is a ferromagnetic semiconductor with a Curie temperature of about 33 K[32]. The Cr^{3+} with three unpaired spins also suggests the expected value of saturation moment of about 3 μ_B[36]. The super-exchange between two Cr ions mediating by the Te ion dominates the intralayer ferromagnetic coupling[32]. The overlapping of the Cr 3d and Te 5p states results in a broadening of Cr bands and a slight polarization of the Te moment[36]. The band structure varies with thickness as most of transition-metal-based semiconductors do, while there will be band modifications driven by ferromagnetic ordering-induced band splitting[37,38]. The narrow Cr-d bands close to the Fermi level are highly correlated and cause the Mott insulating phase above the Curie temperature[37,39]. In the high-temperature paramagnetic phase, there are strong spin–lattice interactions that result in a glassy phase, while strong electronic correlations are also detected in both high and low-temperature regimes[36]. Due to the intense competition from electron correlation effects, which considerably decrease the interlayer ferromagnetic coupling and produce interlayer antiferromagnetic coupling, CST is a system that is located at the boundary between ferromagnetic and A-type antiferromagnetic[37]. Recent studies also displayed the thickness-dependent ferromagnetism and Curie temperature of its nanoflakes[40,41]. Besides the stabilized out-of-plane long-range ordering existing below T_c, there is still in-plane short-range ordering above T_c[42,43]. This short-range ordering is temperature-dependent, which results in a unique change of magnetization and susceptibility[35]. However,

[1]ARC Centre of Excellence in Future Low-Energy Electronics Technologies (FLEET), Monash University, Clayton, VIC 3800, Australia. [2]Department of Materials Science and Engineering, Monash University, Clayton, VIC 3800, Australia. [3]Anhui Province Key Laboratory of Condensed Matter Physics at Extreme Conditions, High Magnetic Field Laboratory, Chinese Academy of Sciences, 230031 Hefei, Anhui, China. [4]Department of Physics, University of Science and Technology of China, 230026 Hefei, People's Republic of China. [5]School of Physics and Materials Science, Anhui University, 230601 Hefei, China. ✉email: Julie.Karel@monash.edu; Kiyonori.Suzuki@monash.edu

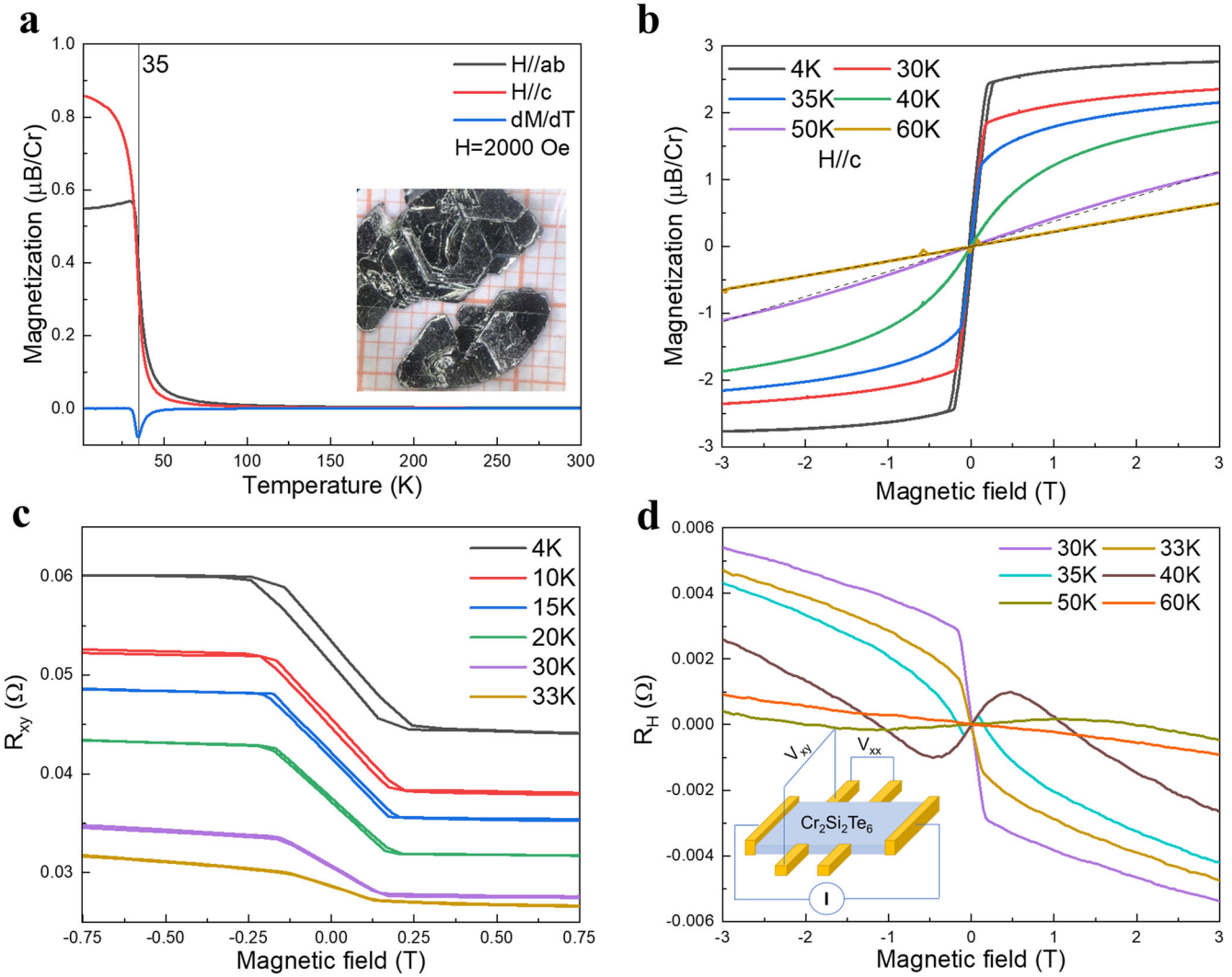

Fig. 1 Characterization of the CST crystal. a Temperature dependence of magnetization along the *c* axis and *ab*-plane, respectively, under field cooling (FC) modes with applied magnetic field 2000 Oe. T_c can be determined as 35 K from dM/dT. Insert: the optical photograph of crystal. The length of the small lattice in the underlayer paper represents 1 mm. **b** The magnetization as a function of the magnetic field when H//*c* axis. The dashed line along the curve at 50 K and 60 K indicates the nonlinear magnetization behavior even till 50 K. **c** Transverse resistance below T_c, which shows a typical AHE hysteresis loop. **d** Hall resistance under the temperature range from 4 K to 60 K, there is a clear change from single band to multiband Hall effect above T_c. The Hall resistance ($\boldsymbol{R}_H$) can be adopted by the standard method $(\boldsymbol{R}_H{}^+ + \boldsymbol{R}_H{}^-)/2$, while $\boldsymbol{R}_H{}^+$ and $\boldsymbol{R}_H{}^-$ represent the resistances measured under opposite applied magnetic field sweep.

how this short-range ordering influences the transport properties of CST remains unclear, particularly for thin layers.

In this work, the thickness-dependent magneto-transport properties of CST nanoflakes demonstrate the unique influence of ferromagnetic correlations. In addition, the as-grown CST bulk crystal presents the same magnetic properties as recent research but with ultra-low resistivity. Owing to this low resistivity, magnetoresistance and Hall effect measurements were performed. Interestingly, the crystal exhibits a nonlinear Hall effect in the low-temperature paramagnetic phase, which has not been found in a 2D ferromagnetic semiconductor system yet. However, this nonlinear Hall effect behavior disappears in thin-layered CST nanoflakes. The coexistence of positive magnetoresistance (PMR) and negative magnetoresistance (NMR) is shown in nanoflakes when the external magnetic field is parallel to the easy axis. The magnetoresistance (MR) behavior and ratio also change with decreasing thickness. Specifically, at temperatures around T_c, there is an obvious drop of the MR ratio in the 12 nm flake at 40 K and a sign reversal from PMR to NMR at 30 K. The extraordinary magneto-transport behavior of CST nanoflakes helps to probe the correlation between ferromagnetic ordering and the electric properties. These findings also provide opportunities to further design special nanoscale spintronic devices based on the 2D ferromagnetic semiconductor.

RESULTS AND DISCUSSION

Characterization of flux-grown single crystal

The CST bulk crystal results will be discussed first. The EDS analysis spectrum and average chemical ratio (Cr: Si: Te = 18: 21: 60) of the platelet indicates that the content of Cr is slightly smaller than in previous reports[34,35]. Some Cr atoms are replaced by Si or Te, but stoichiometry is near ideal for CST. The XRD pattern shows (*006*) and (*0012*) sharp peaks, which indicate that the detecting surface is the *ab*-plane while the direction normal to the surface is the *c* axis. A detailed description of these results is listed in Supplementary Fig. 1. The magnetization as a function of temperature is presented in Fig. 1a. The magnetization under high temperature is similar for both H//*ab*-plane and H// *c* axis, but

obvious separation appears below the Curie temperature. The Curie temperature T_c is obtained from the minimum of the derivative dM/dT curve, which appears at 35 K, close to the calculated value (33 K)[32]. The inset photo of the crystals shows a relatively large size (more than 1 mm in length) with a clean surface obtained after exfoliation of the residual surface cosolvent. The magnetization measurement as a function of the applied magnetic field with H//*c* axis of the CST crystal is performed to ensure the ferromagnetism behavior, as shown in Fig. 1b. The final saturation value of magnetization is close to 2.8 μ_B, which originates from the smaller percentage of Cr content in the crystal. There is still an "S-like" curve at 40 K, deviating from a high-temperature linear relation. The same behavior also happens when H//*ab*-plane, which is shown in Supplementary Fig. 1. This result does not change the T_c but rather suggests the existence of *ab* in-plane short-range ferromagnetic correlations at temperatures greater than T_c[35]. This short-range ordering has also been detected previously using neutron scattering and nonlinear optical polarimetry[32,43]. All of these characteristics demonstrate the high quality of CST crystals, which are appropriate for following transport studies and device design.

The slightly different content of elements also brings differences in transport properties. CST crystals normally show insulating behavior with ultra-large resistance of about 10^9 ohms at liquid helium temperature[34]. However, our self-growth crystals have resistances of less than 0.2 ohms under the same conditions. Although this resistance is ten orders of magnitude smaller than the commonly observed value, the single crystal is still a semiconductor (see supplementary information and Supplementary Fig. 1). The low resistivity likely arises from the impurity energy level generated when the Si or Te atoms replace Cr atoms and form defects. Although materials with impurity levels are sometimes considered to have an imperfection, they can also play an extraordinary role in a particular situation. CST-based devices with ultrahigh resistance are limited in the transport study under low temperatures. Hence, based on the fact that the magnetism is retained, these CST crystals with ultra-low resistance afford the possibility to explore magneto-transport properties even in nanoflakes.

The magnetoresistance effect of this crystal (Supplementary Fig. 2) is similar to previous research[35]. However, this is the first time that the Hall effect of the CST crystal is directly measured.

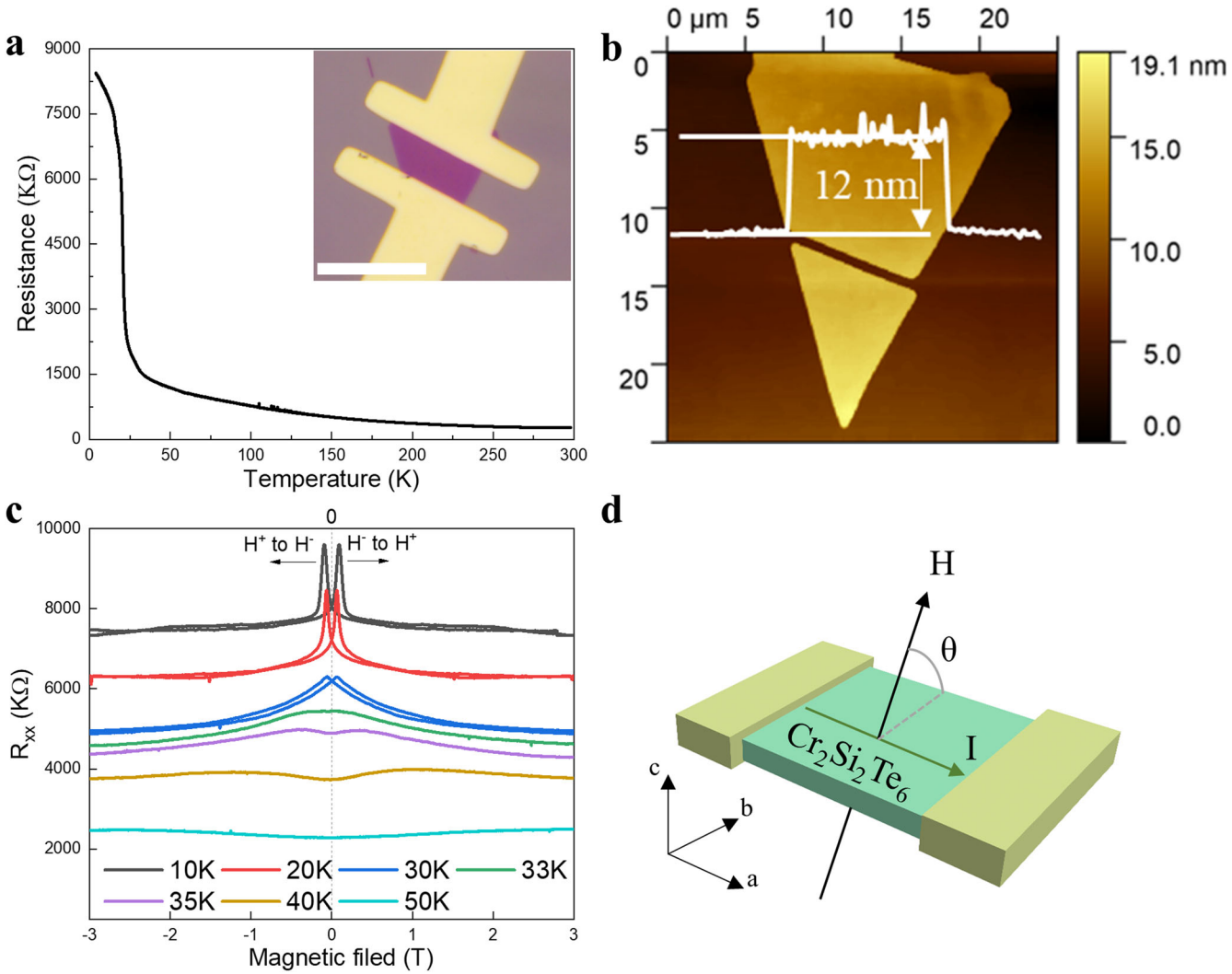

Fig. 2 Temperature-dependent resistance and device morphology. a Temperature-dependent longitudinal resistance of device 1 (D1) based on CST with 12 nm thickness. The applied current is 1 nA. Insert: the optical image of thin-layered CST with a 20 μm scale bar. **b** AFM image and the thickness determination. The thickness is around 12 nm. **c** Longitudinal resistance changes with a magnetic field. Magnetic field H//*c* axis and varies from −3 T to 3 T under different temperatures. Constant current 1 nA is applied. The peak value of resistance appears at ± 0.092 T under 10 K. **d** Schematic of a two-terminal magneto-transport measurement. The angle θ change indicates the magnetic field direction. 0° indicates the H//*ab*-plane, while 90° indicates the H//*c* axis. The magnetic field is perpendicular to the applied current.

Transverse resistance curves (Fig. 1c) show the anomalous Hall hysteresis below T_c. The coercive field increases with decreasing temperature and reaches 260 Oe at 4 K. Peculiarly, the temperature-dependent Hall coefficient in Fig. 1d exhibits a clear sign reversal in a short temperature range starting from T_c to 60 K, forming a nonlinear Hall effect. This nonlinear Hall effect has not been found in other 2D magnets. At 35 K, the sign of the Hall effect will reverse from positive to negative in a low magnetic field range and then go back to positive under a higher external magnet field, forming a protuberance. This protuberance starts to appear at about ±0.1 T for 35 K and significantly shifts to a higher field position with rising temperature. It becomes more obvious at 40 K then trails off near 50 K and finally disappears near 60 K. This nonmonotonic temperature dependence of the Hall effect and unusual sign change around T_c can be normally explained by the two-band character of the electrical transport properties[44]. The Cr d_{z^2} and $d_{x^2-y^2}$ orbitals distribute mainly at the Fermi level of CST which can be included to a two-band model as an example[37]. Specifically, there is a critical fluctuation of ferromagnetic precursors and in-plane short-range order existing above T_c. This short-range order can drive a reconstruction of the Fermi surface and lead to a transition from a single band to a multiband carrier spectrum. This phenomenon has been found previously in antiferromagnet $PdCrO_2$[45]. This could also be an indicator for second order transition of magnetic order, related to the glassy behavior and strong spin–lattice interactions previously seen for CST single crystal[36]. It suggests that short-ranged, two-dimensional magnetic correlations persist to the transition in the temperature range above T_c and cause an anomaly in magnetic susceptibility, and magnetization and may also include the transport properties[36,46]. The temperature range of this nonlinear Hall effect is from 35 to 60 K, which is also the same as the reported characterization of structural distortions in CST crystal corresponding to the short-range ordering[43]. In this temperature range, the MR ratio also simultaneously shows a sudden increase when H//*c* axis (Supplementary Fig. 2a). Hence, these results reflect the effect of short-range ordering on the transport properties of the CST crystal.

Thickness-dependent magnetoresistance

Interestingly, the transport properties of devices with thin-layered CST exhibit numerous differences compared with a single crystal. Figure 2a gives a basic characterization of the device based on a CST nanoflake with a thickness of about 12 nm. It was found that when CST is exfoliated into nanoflakes, the resistance increases in comparison to the bulk crystal and is normally in the range of thousands of kilohms to megohms; this resistance varies with thickness and temperature. While the value of the resistance measured here in the nanoflakes is large, it is still measurable and much smaller in comparison to other reports[47]. The T_c of thin-layered CST with a thickness larger than 10 nm is reported to still be above 30 K[40]. Due to the high resistance, the measurements of longitudinal resistance use a two-probe model. With decreasing temperature, the resistance has a tremendous increase, especially below T_c, which shows a typical semiconductor to insulating characterization. The appearance of devices is shown in the inset while the thickness of about 12 nm is determined by the AFM (Fig. 2b).

The raw data of field-dependent longitudinal resistance is given in Fig. 2c when H//*c* axis. This result displays the clear hysteresis loop of field-dependent resistance and obvious peaks appearing below T_c. These peaks will always be found in the opposite direction of the magnetic field sweep. This phenomenon also appears in the devices with thicker CST flakes (Supplementary Fig. 3a), but the intensity of peaks increases with the reduced thickness of flakes. It can be explained by the domain variation. It has been experimentally verified that the single domain formation will influence the magnetization and coercivity[40]. The domain wall thickness has been calculated as 10 nm, which means that in CST flakes with thickness below this domain walls are difficult to form. Synchronously, thinner flakes have stray field energy lower than the wall energy, also resulting in difficulties to support domain wall formation[40]. The transformation from multidomain to single domain with decreasing thickness will also be reflected in the change of magnetoresistance, besides magnetization. The two sharp maxima in the resistance correspond to the coercive field value where the domain wall density reaches its maximum value (i.e., the domains are all misaligned). As a result, the resistance is maximum due to increased scattering at domain boundaries. A detailed illustration is shown in Supplementary Fig. 3b. Due to the larger coercive field under lower temperatures, it is reasonable to notice that the positions of peaks shift to a higher magnetic field when the temperature goes down.

The thickness-dependent magnetoresistance is collected from devices based on CST flakes with different thicknesses from 12 nm (device 1, D1), 28 nm (device 2, D2) to over 100 nm (Device 3, D3). Figure 3a–c represents the magnetoresistance measured when H//*c* axis and temperature of 30 K, 40 K, and 60 K, respectively. Figure 3d–f is the magnetoresistance measured with H//*ab*-plane. The MR ratio is defined as $\boldsymbol{MR}=\frac{R_H-R_0}{R_0}\times\boldsymbol{100\%}$, where $\boldsymbol{R_H}$ is the resistance as certain magnetic field H, $\boldsymbol{R_0}$ is the resistance at zero magnetic fields. Three temperature points are chosen to identify the MR behavior of CST nanoflakes under different magnetic states. These are 30 K (CST is ferromagnetic), 40 K (CST is paramagnetic), and 60 K (CST is paramagnetic). While 60 K is also the temperature point that CST crystals lose their nonlinear magnetization as well as Hall effect behavior. The MR effect results measured at other temperatures can be found in Supplementary Fig. 4.

At 30 K, a clear change from PMR to NMR is observed with reduced thickness of the CST nanoflakes when H//*c* axis (Fig. 3a). In thick CST flakes (thickness more than 100 nm), the MR ratio increases with increasing magnetic field and maintains a positive value. Although the ferromagnetic interaction and long-range ferromagnetic ordering in CST normally give NMR behavior, the total magnetoresistance effect always has other effects involved, including orbit scattering, electron–electron correlation, and so on[34]. It indicates that even below T_c there is still more than one effect contributing to the resistivity change. For example, the competition of ferromagnetic interactions and orbit scattering from the valence band contribute to the variation from negative to positive MR. In this situation, the orbit scattering may be dominant in the thick layer CST at 30 K. However, with decreasing thickness, the ferromagnetic interaction gradually becomes dominant. Therefore, the MR ratio becomes negative in the 28 nm CST though with a similar curve shape. The peak shapes indicate the reduction of domains. By increasing the applied magnetic field, all spins are already aligned along the magnetic field direction. Then the orbit scattering becomes dominant, and the MR ratio continuously increases. The larger NMR becomes notable in the thinner layer CST (12 nm). The maximum MR in the 12 nm CST can be over 20% at ±3 T and far from saturation. The enhancement of the ferromagnetic interaction in the thinner layer CST may be the most likely cause, originating from a reduction in the number of magnetic domains. Consequently, a larger magnetic field is required to change the spin direction, which results in NMR. Concomitantly, the thin sample results in reduced interlayer coupling, meaning much weaker orbital scattering is generated by the valence band along the *c* axis; this weaker orbital scattering is completely overshadowed by the ferromagnetic interaction. The comprehensive effect results in the MR difference in devices with different thicknesses of CST nanoflakes.

At 40 K, there is large PMR in all three devices but with a different relationship with increasing field. Compared with other temperatures, the MR ratio at 40 K shows a parabolic shape and

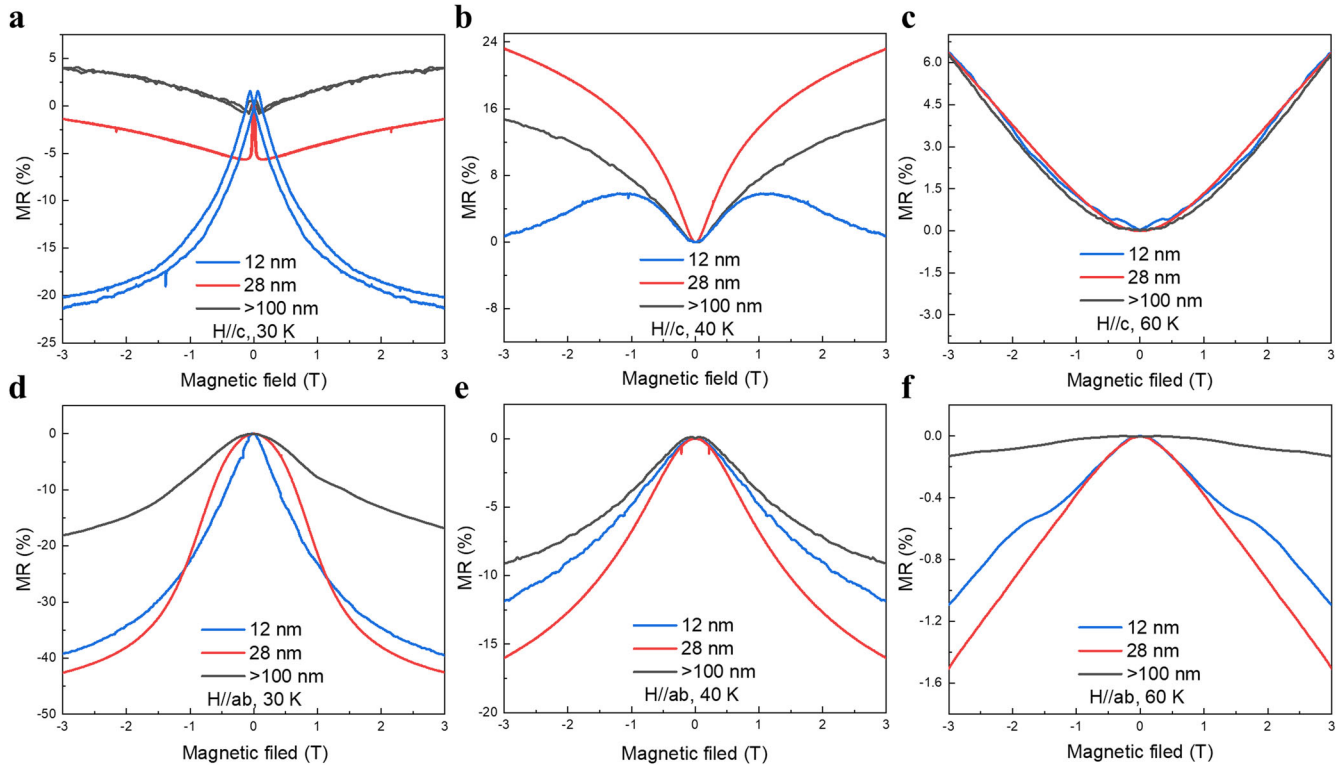

Fig. 3 Thickness-dependent magnetoresistance. a–c The comparison of MR at (**a**) 30 K, (**b**) 40 K, (**c**) 60 K for three $Cr_2Si_2Te_6$-based devices with thickness change from over hundreds of nanometers to 12 nm. External magnetic field H//*c* axis. The peaks appear in the magnetoresistance loop for all devices under T_c. **d–f** The comparison of MR under (**d**) 30 K, (**e**) 40 K, (**f**) 60 K for three $Cr_2Si_2Te_6$-based devices with thickness change from over hundreds of nanometers to 12 nm. External magnetic field H//*ab*-plane.

the largest value. This prominent PMR may also correspond to the mentioned nonlinear Hall effect that has obvious protuberance at 40 K. As shown in Fig. 3b, this PMR ratio firstly increases with decreasing thickness and approaches 24% at ±3 T in 28 nm CST then decreases at 12 nm CST. There are two hump shapes in the MR result of 12 nm CST, different from the thicker CST. The sharp cusp shows a sign of the weak antilocalization (WAL) effect. The WAL effect has already been observed in CST bulk crystal, but have not been verified in its nanoflakes yet[35]. This WAL effect is obvious at 40 K and is still present at 60 K. The WAL effect in CST nanoflakes with different thicknesses and the corresponding magneto-conductivity results were fitted by using the Hikami–Larkin–Nagaoka (HLN) formula. The fitting curve and detailed analysis are listed in the supplementary information (Supplementary Fig. 5). In the 28 nm CST sample, all the magneto-conductivity curves can be fitted well with the HLN model in the low magnetic field range, while the comparatively poor fits obtained for the 12 nm CST sample indicate the weakening of the WAL effect in thin layer CST. The WAL effect normally contributes to PMR but is suppressed by ferromagnetic ordering[35]. Hence, it will not be seen below T_c in ferromagnets. In the CST system, as mentioned, there is in-plane short-range ferromagnetic ordering present even when the temperature is above T_c. Hence, based on these MR results, this in-plane short-range ordering might not affect the existence of the WAL effect in CST when the measurement is along the *c* axis.

At 60 K, there is only a small PMR with no thickness dependence (Fig. 3c). These results are also consistent with the fact that the nonlinear Hall effect disappears at 60 K, potentially implying the absence of short-range ordering above this temperature. In this situation, the PMR only originates from orbit scattering. The details of the variation of this ferromagnetic correlation will be further explained later together with the Hall effect results in the following sections.

When the magnetic field H//*ab*-plane, there is only an NMR effect in all three devices, which can be seen in Fig. 3d–f. The NMR ratio gradually increases with reducing temperature and the highest absolute ratio of MR can reach larger than 40% at only ±3 T. The increase of NMR is nonlinear with an increasing applied magnetic field. It changes rapidly in a low-field region while tending to saturation at the higher magnetic field. Above T_c, there is still a negative MR detected until 60 K, which originates from the magnetic spin fluctuation. Combined with the MR behavior measured when H//*c* direction, this result indicates a typical anisotropic magnetoresistance arising from spin–orbit coupling and appearing in the ferromagnet with out-of-plane magnetism. Additional information is in Supplementary Note 6 and Supplementary Fig. 6. Two interesting points need to be mentioned. One is that a narrower MR curve appears in the 12 nm flake at 30 K. This MR behavior is similar to the result obtained when H//*c* axis, which also corresponds to the mentioned reduction in magnetic domains[40]. Another interesting finding is that the absolute ratio of the NMR first increases and then decreases with decreasing thickness. Hence, the largest NMR ratio always appears at 28 nm CST when the temperature is above T_c. When the temperature is above 60 K, there is almost no MR effect regardless of the applied the magnetic field H direction with respect to the crystal.

Pt/CST hybrid structure and thickness-dependent Hall resistance

Owing to the insulating behavior below T_c and the ultra-large resistance in thin-layered CST, it is still difficult to directly measure the Hall effect from pristine nanoflakes. Hence, hybrid structures of platinum (Pt) and CST with various thicknesses of CST layers are fabricated. The Hall effect results, in this case, can be obtained by

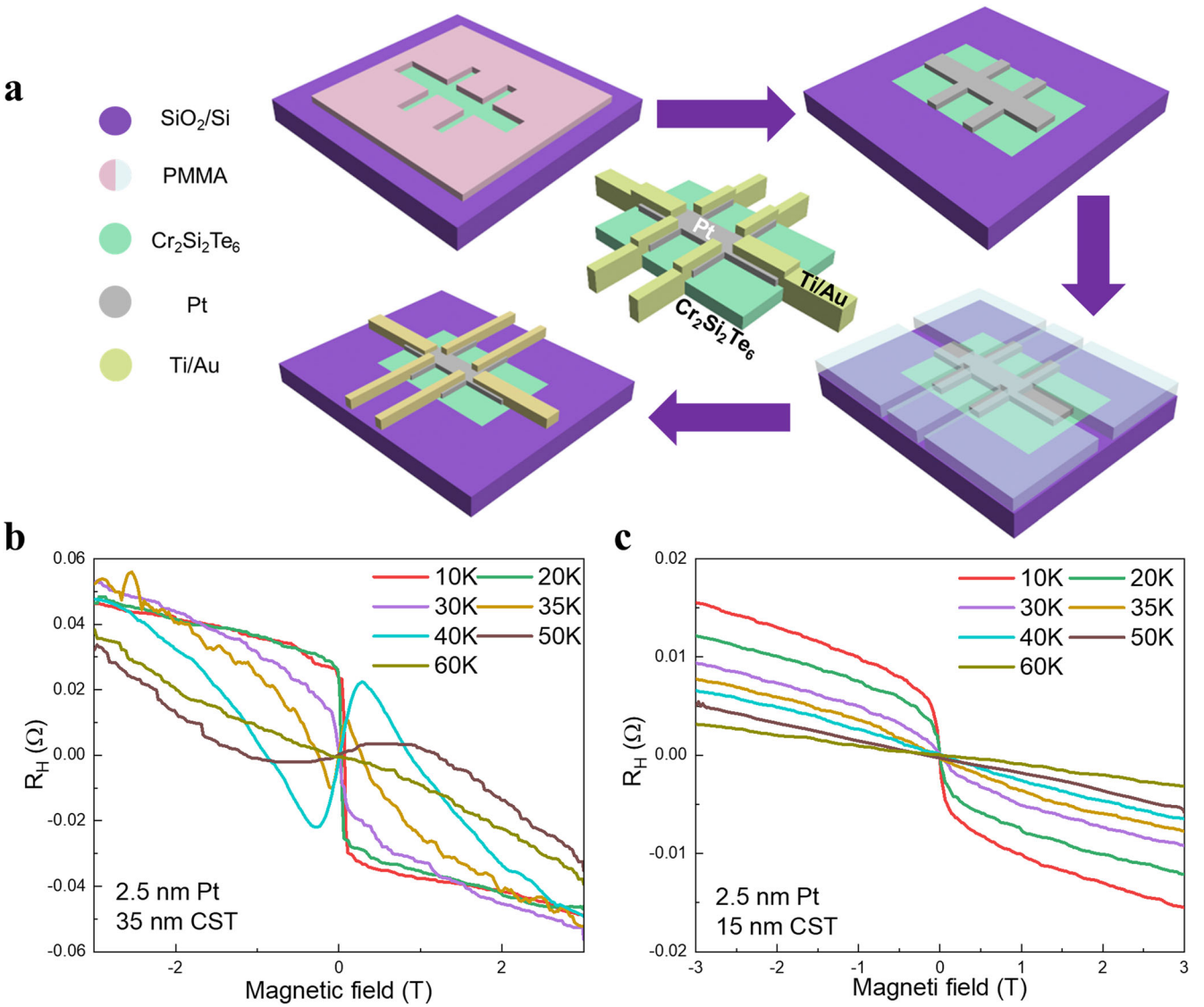

Fig. 4 Transport measurement based on Pt/CST hybrid structure. Pt layer with a thickness of about 2.5 nm is deposited by the PLD system. **a** The flow diagram of fabrication of devices with Pt/CST hybrid structure. **b** Hall resistance of Pt/CST hybrid structure with CST thickness about 35 nm. **c** Hall resistance of Pt/CST hybrid structure with CST thickness about 15 nm.

inducing the proximity effect in the interface of this hybrid structure. Recently, proximity-induced magnetism and anomalous Hall effect have already been studied in numerous 2D magnets[29,30,48,49]. The heavy metal layer (Pt in this work) with strong spin–orbit coupling acquires the spin state as well as transport properties from the underlying 2D magnets. As the flow diagram illustration shows in Fig. 4a, the Hall effect can be measured from the top Pt layer for probing the properties of underlying CST nanoflakes.

The Hall resistances of the Pt/CST hybrid structures with various CST nanoflake thicknesses are shown in Fig. 4b, c, respectively. Device 4 (D4) contains a 2.5 nm Pt layer and a 35 nm CST nanoflake, while device 5 (D5) contains a 2.5 nm Pt layer and a 15 nm CST nanoflake. The device morphology and thickness determination are summarized in Supplementary Fig. 7. The Hall resistances of 35 nm CST are quite similar to the CST bulk crystal, while the only difference is the magnitude. Similar temperature-dependent longitudinal resistance and magnetoresistance can also be observed (Supplementary Fig. 8a). The magnitudes of the MR ratios are smaller than the intrinsic CST nanoflakes, due to the reduced proximity-induced magnetic moment in the Pt atomic layers compared with pristine CST[29]. However, the results indicate that the transport properties from the underlying CST nanoflake are imprinted in the Pt layer due to the proximity effect and mirror the ferromagnetic interaction existing in this hybrid structure.

In the device with a reduced thickness of CST (15 nm), there is still an AHE below 35 K, which means the existence of the proximity effect in this hybrid structure and stabilized long-range ferromagnetic ordering in underlying CST nanoflake. However, there is only a linear Hall effect being observed when the temperature is above T_c. Examination of the Hall resistance of the 15 nm CST above T_c shown in Fig. 4c indicates a possible band structure difference with reducing the thickness of CST. In other words, in this CST nanoflake with a thickness of around 15 nm, the reconstruction of band structure derived by short-range ordering may be restrained. This finding is also consistent with the mentioned MR ratio variation at 40 K. As mentioned previously, there is also a drop in both PMR ratio(H//*c* axis) and NMR ratio(H//*ab*-plane) in thin layer CST (12 nm), which may relate to the variation of short-range ordering. One reasonable speculation of the change in both the MR effect and Hall effect is that the in-plane short-range ordering cannot be stabilized

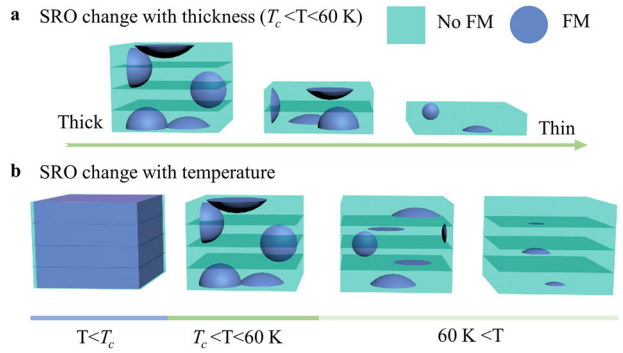

Fig. 5 Illustration of the possible spin ordering process in $Cr_2Si_2Te_6$. The light green regions represent an absence of spin–spin correlations, and the dark blue regions represent ferromagnetic correlations (FM). This spin ordering changes with the thickness (**a**) and temperature (**b**). They are stabilized under T_c as long-range orders and are dynamic as short-range orders above T_c. With the thickness of CST flakes reducing, or the temperature above 60 K, the short-range ordering clusters gradually disappear.

anymore in this thin flake due to the size effect when the temperature is above 35 K.

To better understand the above magneto-transport measurement results that appear in CST nanoflakes with different thicknesses under various temperatures, one of the possible origins is discussed next, along with an explanatory cartoon to assist in the explanation. Combining the experimental results of magnetization, magnetoresistance, and the Hall effect, the ferromagnetic ordering is considered temperature-dependent. Hence, the cartoon in Fig. 5. presents a schematic of the multiple configurations of spin correlation that may exist in ferromagnetic CST as a function of temperature and thickness. As a 2D ferromagnet, CST is unsurprisingly found with stabilized long-range ferromagnetic ordering below T_c, which contributes to the nonlinear magnetization and AHE. This long-range ordering cannot be fully stabilized above T_c, but there may be still short-range ferromagnetic clusters forming due to spin fluctuations. When the temperature is in the range of T_c to 60 K, the deviation of magnetization, large PMR ratio, and nonlinear Hall effect, simultaneously imply that the existence of this short-range order in the CST crystal and thicker exfoliated layers is possible. These short-range order clusters transform from three-dimensional to two-dimensional, then become weaker, and finally vanish when the temperature further increases and is above 60 K[43]. Hence, both magnetizations and Hall resistances only exhibit linearly field-dependent behavior, while almost no MR can be detected above 60 K.

Based on the thickness-dependent magneto-transport results of CST nanoflakes, these short-range ordering clusters are also likely to change with thickness. As mentioned in Fig. 3, the absolute MR ratio tends to decrease with further reducing thickness to 12 nm. While the WAL effect in D1 even cannot be suppressed. Therefore, there is a high possibility that the in-plane short-range ordering firstly becomes stronger when the dimension of CST changes from 3D to 2D (crystal to 28 nm flake). However, with thickness further reducing, the short-range ordering clusters cannot be maintained. It may also vary from 3D short-range ordering clusters to 2D and finally disappear in thin layer CST. The absence of the nonlinear Hall effect in 15 nm CST (Fig. 4c) also becomes powerful evidence to support the vanishing of these short-range order clusters in thin layer CST. As a vdW material, the interlayer and intralayer spin correlations will be affected by the number of layers, especially in CST which is reported to have intralayer ferromagnetic and interlayer antiferromagnetic coupling. At temperatures above T_c, the interplay of short-range magnetic correlations and electronic interactions may also provide the possibility to generate peculiar transport properties, since the enhanced electronic repulsion appears in particular at low dimensions[50]. The competition effect in this temperature range (T_c to 60 K) may also manifest as the change of band structure, leading to the abnormal transport properties in thin layer CST. This is a comprehensive analysis based on the current magneto-transport results of CST-based nanodevices, but it still requires subsequent experimental or theoretical confirmation. Although magneto-transport measurements are one approach to probing the spin states of materials, the exact detection or calculation of spin correlations especially in low-dimensional nanoflakes requires further verification.

In conclusion, we have grown a CST crystal with ultra-low resistivity while still maintaining ferromagnetism, which gives the possibility for further magneto-transport measurements in nanoflakes. There are unique thickness-dependent magneto-transport properties in CST. Nonmonotonic thickness-dependent MR effects can be detected at different temperature intervals with T_c and 60 K as the two cut-off points. In the temperature range from T_c to 60 K, different from the nonlinear Hall effect in CST crystal, the thin layer CST only exhibits the linear Hall effect. These magneto-transport properties may be mainly attributed to the variation of spin correlations with changing temperature and thickness, and there are also several competitive effects, including orbit scattering and electronic interactions. It is the first time to explore the intrinsic Hall effect of 2D ferromagnetic semiconductors and characterize the thickness-dependent magneto-transport properties of CST nanoflakes. These results exhibit the possible relationship between short-range ordering and magneto-transport properties of CST, which may also be able to facilitate research on other 2D ferromagnets. The analysis of spin correlation and abnormal magneto-transport properties makes this work a pioneer for future investigation of the CST-based nanodevice and its possible spintronic applications.

EXPERIMENTAL METHODS

Materials synthesis and devices fabrication

CST single crystals were synthesized by flux growth. A mixture of high purity Chromium particles (99.95%), Silicon particles (99.999%), and Tellurium powder (99.999%) were sealed in an evacuated silica tube with the quartz wool mounted on top of the tube. The molar ratio of Cr: Si: Te is 1:3:15, in which Te functions as the flux. The tube was heated up to 1000 °C in the furnace and kept for 10 h, all the materials were melted into homogeneous liquids and then naturally cooled down followed by centrifugation to separate the extra flux and crystal. Then the plate-like crystals with silvery luster and a few millimeters in size can be picked out from the bottom of the tube.

The nanoflakes of CST were mechanically exfoliated from the single crystals to the surface of polydimethylsiloxane (PDMS) sheets by using blue scotch tape. Selected flakes were transferred onto the surface of the SiO_2/Si substrates by the target dry transfer method. All these processes proceeded in the glove box filled with argon (O_2 and H_2O < 0.01 ppm) to avoid the influence of air contamination and oxidation.

As for magneto-transport device fabrication, the substrates were covered with a spin-coated polymethyl methacrylate (PMMA) resist, and then patterned by electron-beam lithography (EBL) to define the source-drain contacts. Metal contacts with 8 nm Ti and 80 nm Au were deposited by electron-beam evaporation in a vacuum (5×10^{-5} Torr). Following by lift-off process, the CST-based devices with electrodes on top of the flakes were obtained. The Pt/CST hybrid structure devices with an additional procedure of platinum (Pt) layer deposition. After being spin-coated with PMMA resist, Hall-bar-shaped patterns were first drawn by EBL. The Pt layer with a thickness of 2.5 nm then was deposited by pulsed laser deposition (PLD) immediately to avoid

exposure to air. The laser energy used is ~150 mJ, the deposition time is around 110 s, and the target distance is settled as 7 cm. Then the metal contacts were deposited onto the Pt layer in the same way as pristine CST devices.

Crystal and nanoflakes characterization

The structure and quality of CST single crystal were characterized by several methods, including X-ray diffraction (XRD) with Cu Kα ($\lambda = 0.1542$ nm) radiation, energy dispersive spectrometer (EDS), and Raman spectrum. The surface topographies of CST nanodevices were characterized by optical microscopy (Nikon Instrument) and atomic force microscopy (AFM).

Physical property measurements

The magnetization measurements of CST single crystals were performed in a Quantum Design MPMS-XL3 system (SQUID). The magneto-transport properties of a single crystal were performed in a Quantum Design PPMS system (PPMS®DynaCool™) using Horizontal Rotator Option. The gold-plated copper wires were adhered to both crystal surface and chip hold using the silver paste. The four-terminal method was used for measuring the magnetoresistance with the applied current of 1 mA.

The magneto-transport property measurements of nanodevices were also performed in the same equipment but replacing the silver paste adhesion with a wire bonding process (FS Bondtec with Series 58 Wedge). The devices with Pt/CST hybrid structure use the four-terminal method with the applied current of 1 μA. As for the magnetoresistance measurement of pristine CST nanoflakes, the two-terminal method was adopted due to the ultrahigh resistivity of nanoflakes. Devices were measured by using an ultrasensitive Keysight B2912A fA source meter with an applied current of 1–10 nA.

DATA AVAILABILITY

The data that support the findings of this study are available from the corresponding author upon reasonable request.

Received: 9 November 2022; Accepted: 18 May 2023;
Published online: 01 June 2023

REFERENCES

1. Huang, B. et al. Layer-dependent ferromagnetism in a van der Waals crystal down to the monolayer limit. *Nature* **546**, 270 (2017).
2. Gong, C. et al. Discovery of intrinsic ferromagnetism in two-dimensional van der Waals crystals. *Nature* **546**, 265 (2017).
3. Tan, C. et al. Hard magnetic properties in nanoflake van der Waals Fe_3GeTe_2. *Nat. Commun.* **9**, 1554 (2018).
4. May, A. F. et al. Ferromagnetism near room temperature in the cleavable van der Waals crystal Fe_5GeTe_2. *ACS Nano* **13**, 4436–4442 (2019).
5. Bonilla, M. et al. Strong room-temperature ferromagnetism in VSe_2 monolayers on van der Waals substrates. *Nat. Nanotechnol.* **13**, 289–293 (2018).
6. Tiwari, S., Van de Put, M. L., Soree, B. & Vandenberghe, W. G. Critical behavior of the ferromagnets CrI_3, $CrBr_3$, and $CrGeTe_3$ and the antiferromagnet $FeCl_2$: a detailed first-principles study. *Phys. Rev. B* **103**, 014432 (2021).
7. Zhang, Z. et al. Direct photoluminescence probing of ferromagnetism in monolayer two-dimensional CrBr3. *Nano Lett.* **19**, 3138–3142 (2019).
8. Yi, M. & Shen, Z. A review on mechanical exfoliation for the scalable production of graphene. *J. Mater. Chem. A* **3**, 11700–11715 (2015).
9. Cortie, D. L. et al. Two-dimensional magnets: forgotten history and recent progress towards spintronic applications. *Adv. Funct. Mater.* **30**, 1901414 (2020).
10. Li, H., Ruan, S. & Zeng, Y.-J. Intrinsic Van Der Waals magnetic materials from bulk to the 2D limit: new frontiers of spintronics. *Adv. Mater.* **31**, 1900065 (2019).
11. Wan, Z. et al. Self-powered $MoSe_2$/ZnO heterojunction photodetectors with current rectification effect and broadband detection. *Mater. Des.* **212**, 110185 (2021).
12. Jiang, S., Li, L., Wang, Z., Mak, K. F. & Shan, J. Controlling magnetism in 2D CrI_3 by electrostatic doping. *Nat. Nanotechnol.* **13**, 549–553 (2018).
13. Li, X., Wu, X. & Yang, J. Half-metallicity in $MnPSe_3$ exfoliated nanosheet with carrier doping. *J. Am. Chem. Soc.* **136**, 11065–11069 (2014).
14. Yan, Z. et al. Emerging two-dimensional tellurene and tellurides for broadband photodetectors. *Small* **18**, 2200016 (2022).
15. Lv, P., Li, Y.-L. & Wang, J.-F. Monolayer Ti 2 C MXene: manipulating magnetic properties and electronic structures by an electric field. *Phys. Chem. Chem. Phys.* **22**, 11266–11272 (2020).
16. Mu, H., Yu, W., Yuan, J., Lin, S. & Zhang, G. Interface and surface engineering of black phosphorus: a review for optoelectronic and photonic applications. *Mater. Futures* **1**, 012301 (2022).
17. Yu, W. et al. Flexible 2D materials beyond graphene: synthesis, properties, and applications. *Small* **18**, 2105383 (2022).
18. Deng, Y. et al. Gate-tunable room-temperature ferromagnetism in two-dimensional Fe3GeTe2. *Nature* **563**, 94–99 (2018).
19. Seyler, K. L. et al. Ligand-field helical luminescence in a 2D ferromagnetic insulator. *Nat. Phys.* **14**, 277–281 (2018).
20. Xie, L. et al. Ultrasensitive negative photoresponse in 2D $Cr_2Ge_2Te_6$ photodetector with light-induced carrier trapping. *Nanotechnology* **29**, 464002 (2018).
21. Zhuo, W. et al. Manipulating ferromagnetism in few-layered $Cr_2Ge_2Te_6$. *Adv. Mater.* **33**, 2008586 (2021).
22. Zhang, L. et al. Proximity-coupling-induced significant enhancement of coercive field and curie temperature in 2D van der Waals heterostructures. *Adv. Mater.* **32**, 2002032 (2020).
23. Rahman, S., Liu, B., Wang, B., Tang, Y. & Lu, Y. Giant photoluminescence enhancement and resonant charge transfer in atomically thin two-dimensional Cr_2Ge2Te_6/WS_2 heterostructures. *ACS Appl. Mater. Interfaces* **13**, 7423–7433 (2021).
24. Wang, Z. et al. Very large tunneling magnetoresistance in layered magnetic semiconductor CrI_3. *Nat. Commun.* **9**, 2516 (2018).
25. Song, T. et al. Giant tunneling magnetoresistance in spin-filter van der Waals heterostructures. *Science* **360**, 1214–1218 (2018).
26. Kim, H. H. et al. One million percent tunnel magnetoresistance in a magnetic van der Waals heterostructure. *Nano Lett.* **18**, 4885–4890 (2018).
27. Escolar, J. et al. A Anisotropic magnetoconductance and Coulomb blockade in defect engineered $Cr_2Ge_2Te_6$ van der Waals heterostructures. *Phys. Rev. B* **100**, 054420 (2019).
28. Ostwal, V., Shen, T. & Appenzeller, J. Efficient spin-orbit torque switching of the semiconducting Van Der Waals ferromagnet $Cr_2Ge_2Te_6$. *Adv. Mater.* **32**, 1906021 (2020).
29. Lohmann, M. et al. Probing magnetism in insulating $Cr_2Ge_2Te_6$ by induced anomalous Hall effect in Pt. *Nano Lett.* **19**, 2397–2403 (2019).
30. Zhong, D. et al. Layer-resolved magnetic proximity effect in van der Waals heterostructures. *Nat. Nanotechnol.* **15**, 187–191 (2020).
31. Liu, Y. et al. The environmental stability characterization of exfoliated few-layer $CrXTe_3$ (X= Si, Ge) nanosheets. *Appl. Surf. Sci.* **511**, 145452 (2020).
32. Williams, T. J. et al. Magnetic correlations in the quasi-two-dimensional semiconducting ferromagnet $CrSiTe_3$. *Phys. Rev. B* **92**, 144404 (2015).
33. Liu, Y. & Petrovic, C. Anisotropic magnetic entropy changes in $Cr_2X_2Te_6$ (X= Si and Ge). *Phys. Rev. Mater.* **3**, 014001 (2019).
34. Li, Z. et al. Coexistence of large positive and negative magnetoresistance in $Cr_2Si_2Te_6$ ferromagnetic semiconductor. *Sci. China Mater.* **65**, 780–787 (2021).
35. Zhang, Z., Wang, Z. & Zhang, Z. Magneto-transport and weak anti-localization in ferromagnetic semiconductor $CrSiTe_3$ single crystal. *Appl. Phys. Lett.* **113**, 142404 (2018).
36. Casto, L. D. et al. Strong spin-lattice coupling in $CrSiTe_3$. *APL Mater.* **3**, 041515 (2015).
37. Zhang, J. et al. Unveiling electronic correlation and the ferromagnetic superexchange mechanism in the van der Waals Crystal $CrSiTe_3$. *Phys. Rev. Lett.* **123**, 047203 (2019).
38. Rui, X. et al. Advanced atomic force microscopies and their applications in two-dimensional materials: a review. *Mater. Futures* **1**, 032302 (2022).
39. Siberchicot, B., Jobic, S., Carteaux, V., Gressier, P. & Ouvrard, G. Band structure calculations of ferromagnetic chromium tellurides $CrSiTe_3$ and $CrGeTe_3$. *J. ChemInform.* **27**, 5863–5867 (1996).
40. Zhang, C. et al. Hard ferromagnetic behavior in atomically thin $CrSiTe_3$ flakes. *Nanoscale* **14**, 5851–5858 (2022).
41. Zhang, C. et al. Pressure-enhanced ferromagnetism in layered CrSiTe3 flakes. *Nano Lett.* **21**, 7946–7952 (2021).
42. Carteaux, V., Moussa, F. & Spiesser, M. 2D Ising-like ferromagnetic behaviour for the lamellar $Cr_2Si_2Te_6$ compound: a neutron scattering investigation. *EPL* **29**, 251 (1995).
43. Ron, A., Zoghlin, E., Balents, L., Wilson, S. D. & Hsieh, D. Dimensional crossover in a layered ferromagnet detected by spin correlation driven distortions. *Nat. Commun.* **10**, 1654 (2019).
44. Gonzalez, P., Agapito, J. & Pardo, D. Two-band model parameters deduced from Hall coefficient measurements in polycrystalline films of SnTe. *J. Phys. C: Solid State Phys.* **19**, 899 (1986).

45. Daou, R., Frésard, R., Hébert, S. & Maignan, A. Impact of short-range order on transport properties of the two-dimensional metal $PdCrO_2$. *Phys. Rev. B* **92**, 245115 (2015).
46. McGuire, M. A. et al. Magnetic behavior and spin-lattice coupling in cleavable van der Waals layered $CrCl_3$ crystals. *Phys. Rev. Mater.* **1**, 014001 (2017).
47. Lin, M.-W. et al. Ultrathin nanosheets of $CrSiTe_3$: a semiconducting two-dimensional ferromagnetic material. *J. Mater. Chem. C.* **4**, 315–322 (2016).
48. Yao, X. et al. R Record high-proximity-induced anomalous Hall effect in $(Bi_xSb_{1-x})_2Te_3$ thin film grown on $CrGeTe_3$ substrate. *Nano Lett.* **19**, 4567–4573 (2019).
49. Gupta, V. et al. Manipulation of the van der Waals magnet $Cr_2Ge_2Te_6$ by spin–orbit torques. *Nano Lett.* **20**, 7482–7488 (2020).
50. Sivadas, N., Daniels, M. W., Swendsen, R. H., Okamoto, S. & Xiao, D. Magnetic ground state of semiconducting transition-metal trichalcogenide monolayers. *Phys. Rev. B* **91**, 235425 (2015).

ACKNOWLEDGEMENTS

This study was supported by the Natural Science Foundation of China No. U19A2093. This study was also supported in part through the Australian Research Council Centre of Excellence in Future Low Energy Electronics Technologies under CE170100039 and the Australian Research Council Discovery Project DP200102477 and DP220103783. This work was performed in part at the Melbourne Centre for Nanofabrication (MCN) in the Victorian Node of the Australian National Fabrication Facility (ANFF).

AUTHOR CONTRIBUTIONS

Y.L., J.K., and K.S. conceived and designed the study. Y.L. performed most of the experiments, including nanodevice fabrication, characterization, transport measurement, and data analysis. Z.C. and J.W. provide the single crystal. T.L. performed PLD. Y.L. wrote the manuscript. M.L.T., J.K., and K.S. give advice for the manuscript. All authors have given approval to the final version of the manuscript.

COMPETING INTERESTS

The authors declare no competing interests.

ADDITIONAL INFORMATION

Supplementary information The online version contains supplementary material available at https://doi.org/10.1038/s41699-023-00404-1.

Correspondence and requests for materials should be addressed to Julie Karel or Kiyonori Suzuki.

Reprints and permission information is available at http://www.nature.com/reprints

Publisher's note Springer Nature remains neutral with regard to jurisdictional claims in published maps and institutional affiliations.